Photon regions, shadow observables and constraints from M87* of a Kerr-Newman-like black hole in Bumblebee gravity surrounded by plasma*

Jian-Peng Zhang (张健鹏) Yu Zhang (张钰)† Li Han (韩力)

Faculty of Science, Kunming University of Science and Technology, Kunming 650500, China

Abstract: In this paper, we investigate the photon regions, shadow, and observational constraints of a Kerr-Newman-like black hole in Bumblebee gravity within a plasma medium. Using a specific non-homogeneous power-law plasma model to ensure the separability of the Hamilton-Jacobi equation, we derive the null geodesic equations, analyze the photon regions, and construct the black hole shadow. Furthermore, we introduce two sets of shadow observables to systematically analyze the distinct effects of each physical parameter (spin a, charge Q_0, Lorentz-violating parameter ℓ, and plasma parameter k) on the shadow geometry. Specifically, we find that a and ℓ mainly enhance the distortion of the shadow, whereas Q_0 and k primarily lead to radial shrinkage. In addition, a brief evaluation of the energy emission rate shows that increasing these parameters generally suppresses the emission peak. Finally, by modeling M87* as a charged, rotating black hole in Bumblebee gravity surrounded by plasma, we constrain the physical parameters using observations from the Event Horizon Telescope (EHT). For a fixed viewing angle of 17°, the angular diameter $\theta_d = 42 \pm 3\,\mu$as narrows the viable parameter space, while the circularity deviation $\Delta C \lesssim 0.1$ and axis ratio $1 < D_x \lesssim 4/3$ satisfy the EHT limits. This suggests that the charged, rotating black hole in Bumblebee gravity surrounded by plasma may be a candidate for real astrophysical black holes.

Keywords: black hole shadow, Bumblebee gravity, plasma, EHT

DOI: 10.1088/1674-1137/ae8cf0 **CSTR:** 32044.14.ChinesePhysicsC.50115101

I. INTRODUCTION

The successful imaging of M87* [1−6] and Sgr A* [7−9] by the Event Horizon Telescope (EHT) collaboration marks a new era in which black hole astrophysics enters the realm of testing strong-gravity theories through direct imaging [10−12]. The black hole shadow, characterized by a central dark region surrounded by a bright ring, is, in essence, the optical projection of the spacetime geometry near the black hole onto the celestial sphere of a distant observer. Although current EHT observations are highly consistent with the predictions of Kerr black holes in General Relativity (GR) within their uncertainties [5, 13], they still leave room for exploring new physics beyond GR within the current observational precision, such as dark matter [14−16], modified gravity theories [17−19], and quantum gravity effects [20−22].

Against this backdrop, using black hole shadows to test potential deviations from GR has become one of the most important avenues for studying modified gravity theories [23−28]. Among the various candidate theories, those involving Lorentz symmetry breaking (LSB) have attracted considerable attention because of their clear physical motivations [29−34]. Although Lorentz symmetry is a fundamental cornerstone of both quantum field theory and GR, its strict validity at all energy scales remains an open question. Various candidate theories of quantum gravity predict that this symmetry may be broken at high-energy scales [35, 36], leaving observable effects in low-energy effective theories [37]. To systematically characterize such LSB effects, Kostelecky *et al.* [38] developed the Standard Model Extension, providing a unified framework for describing Lorentz violation. In the gravity sector, the Einstein-Bumblebee model stands as one of the simplest implementations of the Standard Model Extension [35, 39, 40]. It induces spontaneous LSB by introducing a vector field with a non-zero vacuum expectation value, thereby generating the Lorentz-violating parameter ℓ in the low-energy effective field theory to characterize the strength of this symmetry breaking.

It is worth noting that this Lorentz-violating parameter ℓ has been subject to rigorous observational constraints across various astrophysical scales. For instance, Casana *et al.* [41] constrained this parameter using classical Solar System tests. In the strong-field regime, Liang *et al.* [42] probed the vector hair of black holes via ex-

Received 29 April 2026; Accepted 16 July 2026; Accepted manuscript online 17 July 2026

* The work was supported by Yunnan Xingdian Talent Support Program-Young Talent Project

† E-mail: zhangyu_128@126.com

©2026 Chinese Physical Society and the Institute of High Energy Physics of the Chinese Academy of Sciences and the Institute of Modern Physics of the Chinese Academy of Sciences and IOP Publishing Ltd. All rights, including for text and data mining, AI training, and similar technologies, are reserved.

treme-mass-ratio inspirals. Furthermore, Kumar *et al.* [43] investigated Lorentz symmetry violation through strong- and weak-lensing observables of rotating black holes, while Qi *et al.* [44] placed bounds on ℓ by analyzing the orbital precession of the S2 star around the galactic center. In recent years, Schwarzschild-like [41, 45, 46] and Kerr-like black hole solutions [47−50] have been derived within this framework and used to investigate horizon structures and photon geodesic properties. However, most existing studies of bumblebee black hole shadows are confined to vacuum conditions [51−57], neglecting the potentially significant effects of realistic astrophysical environments.

On the other hand, even without invoking corrections to GR, the interpretation of shadow observations is still strictly constrained by environmental factors. In realistic astrophysical scenarios, black holes are surrounded by accretion flows, jets, or the interstellar medium [58, 59], which on macroscopic scales can be effectively modeled as a plasma medium. As noted in previous studies [60, 61], the dispersive properties of plasma modify the photon dispersion relation, causing their trajectories to deviate from the standard vacuum null geodesics. In this context, the pioneering work of Atamurotov *et al.* [62] systematically formulated the theoretical framework describing plasma effects on black hole shadows. Subsequent research [63−68] has shown that, whether the plasma distribution is homogeneous or non-homogeneous, the primary consequence is a systematic reduction in the shadow's apparent size, accompanied by deformations in its shape.

Current research on this problem has primarily proceeded along two paths: one investigates the impact of modified gravity theories on black hole shadows, but is often confined to vacuum conditions [69−73], while the other analyzes plasma correction effects, but strictly within the framework of GR [74−82]. Consequently, for scenarios incorporating both modified gravity effects and realistic plasma environments [83−85], systematic analyses of black hole shadows and their observables within a unified theoretical framework remain relatively limited.

In this paper, we investigate a Kerr-Newman-like (KN-like) black hole in Bumblebee gravity, immersed in a non-homogeneous plasma background. It is worth noting the astrophysical feasibility of the charge parameter in realistic environments. Specifically, the Wald effect [86] demonstrates that a rotating black hole immersed in an external magnetic field naturally acquires a net charge, while differential accretion of ions and electrons can similarly lead to the accumulation of a non-zero net charge [87]. Inspired by the EHT collaboration [88], which constrained the effective charge of M87* by modeling it as a phenomenological parameter, we adopt a similar approach to explore the shadow and parameter constraints of this charged black hole. To ensure computational feasibility while maintaining physical consistency, we adopt a radial power-law non-homogeneous plasma model that preserves the separability of the Hamilton-Jacobi equation. The horizons, null geodesic equations, and photon region of the black hole are obtained. Within this framework, we systematically calculate the shadow and introduce two sets of shadow observables to characterize the influence of various physical parameters. Furthermore, using the EHT observations of M87* — specifically the angular diameter, axial ratio, and circularity deviation — we place stringent constraints on the parameter space of this coupled model. This enables us to test the viability of the KN-like black hole as an M87* candidate within a realistic plasma environment. Therefore, the focus of our work is to combine Bumblebee gravity with a plasma environment to systematically investigate the black hole shadow characteristics of this coupled model.

This paper is structured as follows: In Sec. II, we introduce the metric of the KN-like black hole and discuss its horizons and the allowed parameter range. Sec. III derives the null geodesic equations in the presence of plasma and subsequently analyzes the corresponding photon regions to determine the shadow boundary. Sec. IV presents the black hole shadows and characterizes how the shadow shape and observables respond to parameter variations, while also providing a brief evaluation of the associated energy emission rate. In Sec. V, we impose constraints on the model parameters by confronting our theoretical results with the EHT observational data. Finally, a summary is provided in Sec. VI. Throughout this paper, unless otherwise specified, we employ geometric units where $G = c = M = 1$ and adopt the metric signature (–, +, +, +).

II. BLACK HOLE WITHIN THE FRAMEWORK OF BUMBLEBEE GRAVITY

The black hole solution considered in this paper is based on Bumblebee gravity theory. In this theory [35, 39, 40], a vector field B_u with a non-zero vacuum expectation value is introduced to induce spontaneous Lorentz symmetry breaking (LSB) in the gravitational interaction. As a result, a parameter characterizing the symmetry-breaking strength appears in the low-energy effective field theory. In this work, we adopt the stationary, axisymmetric, and charged Kerr-Newman-like (KN-like) black hole solution recently obtained by Liu *et al.* [89]. In Boyer-Lindquist coordinates, the metric is given by

$$\begin{aligned} \mathrm{d}s^2 =& -\frac{\Delta_r}{\rho^2}\left(\mathrm{d}t - a\sqrt{1+\ell}\sin^2\theta\,\mathrm{d}\phi\right)^2 \\ &+ (1+\ell)\frac{\rho^2}{\Delta_r}\mathrm{d}r^2 + \rho^2\mathrm{d}\theta^2 \\ &+ \frac{\sin^2\theta}{\rho^2}\left(a\sqrt{1+\ell}\,\mathrm{d}t - \left(r^2 + a^2(1+\ell)\right)\mathrm{d}\phi\right)^2, \end{aligned} \tag{1}$$

where the relevant metric functions are defined as follows:

$$\Delta_r = (1+\ell)a^2 + r^2 - 2Mr + \frac{2(1+\ell)Q_0^2}{2+\ell},$$
$$\rho^2 = r^2 + (1+\ell)a^2\cos^2\theta. \tag{2}$$

Here, M denotes the black hole mass, a represents the spin parameter, and Q_0 is the charge parameter. The Lorentz-violating parameter ℓ characterizes the strength of the LSB. In the limit $\ell \to 0$, the metric reduces to the Kerr-Newman solution of general relativity. If we further set $Q_0 \to 0$, it recovers the standard Kerr black hole solution.

The horizons of a black hole are determined by the roots of its radial metric function, which satisfy

$$\Delta_r = (1+\ell)a^2 + r^2 - 2Mr + \frac{2(1+\ell)Q_0^2}{2+\ell} = 0. \tag{3}$$

This equation admits three types of root structure: two distinct positive real roots, one double positive root, and no positive real roots. Specifically, the existence of two distinct positive real roots corresponds to a black hole with an event horizon and a Cauchy horizon. When the two roots coincide, the black hole becomes extremal. Finally, if no positive real roots exist, the horizon disappears and the spacetime evolves into a naked singularity. Figure 1 presents the boundaries of the extremal black hole in the (ℓ, a) and (Q_0, a) parameter planes. It is evident that as the charge parameter Q_0 or the Lorentz-violating parameter ℓ increases, the allowed range of the spin parameter a shrinks.

Figure 2 shows the behavior of the radial metric function $\Delta_r(r)$ as a function of the radial coordinate for different parameter combinations. The intersections of the curves with the r-axis correspond to the horizon positions, where the left and right intersections represent the Cauchy horizon and the event horizon, respectively, whereas the tangent point corresponds to the extremal black hole case. It can be seen that increasing the spin parameter a, the charge parameter Q_0, or the Lorentz-violating parameter ℓ causes the Cauchy horizon and the event horizon to approach each other. Based on the above analysis, all subsequent calculations of the black hole shadow are restricted to the parameter region that ensures the existence of the event horizon.

III. NULL GEODESICS AND PHOTON REGIONS IN A PLASMA ENVIRONMENT

To investigate the joint effects of Lorentz symmetry breaking (LSB) in Bumblebee gravity and the plasma environment on the shadow structure, it is necessary to characterize photon propagation and photon regions in this background. Since the spacetime under consideration is stationary and axisymmetric, the photon motion problem can be formulated as a Hamiltonian dynamical system with conserved quantities. In the study of shadows from axisymmetric black holes, the Hamilton-Jacobi (H-J) equation is widely used because of its variable separability.

However, the introduction of a plasma medium causes the photon dispersion relation to deviate significantly from the vacuum case, generally destroying the separability of the H-J equation. Therefore, it is crucial to select a plasma model that has clear astrophysical motivation while preserving the separability of the H-J equation. This paper employs a specific non-homogeneous power-law plasma model, derives the null geodesic equations of photons on this basis, and analyzes the photon regions, thereby laying the foundation for the subsequent construction of black hole shadows.

In the vacuum background, the motion of photons is described by the H-J equation:

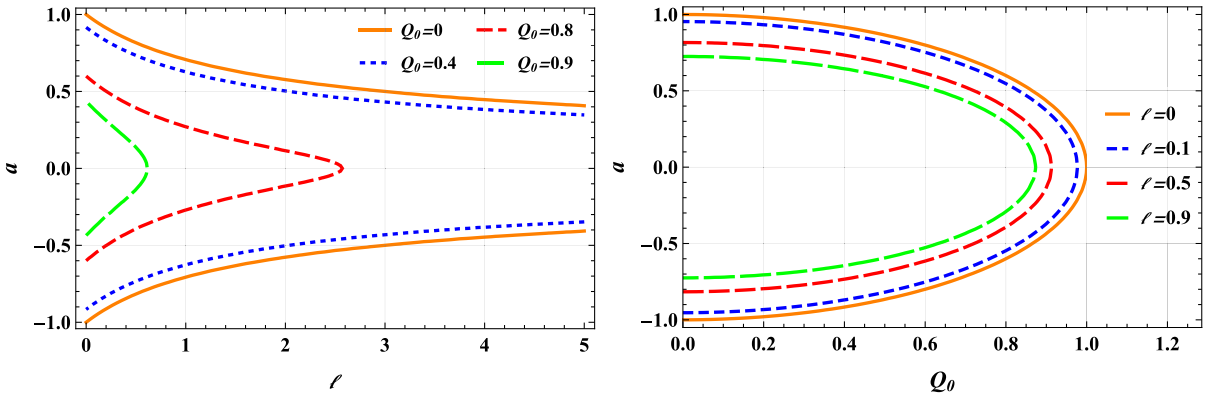


Fig. 1. (color online) Parameter space of the Bumblebee black hole ($M = 1$). The boundary curves represent the extremal black hole condition, corresponding to the degenerate roots of the radial metric function. The region enclosed by the curves denotes the parameter space in which an event horizon exists, whereas the exterior region corresponds to naked singularities.

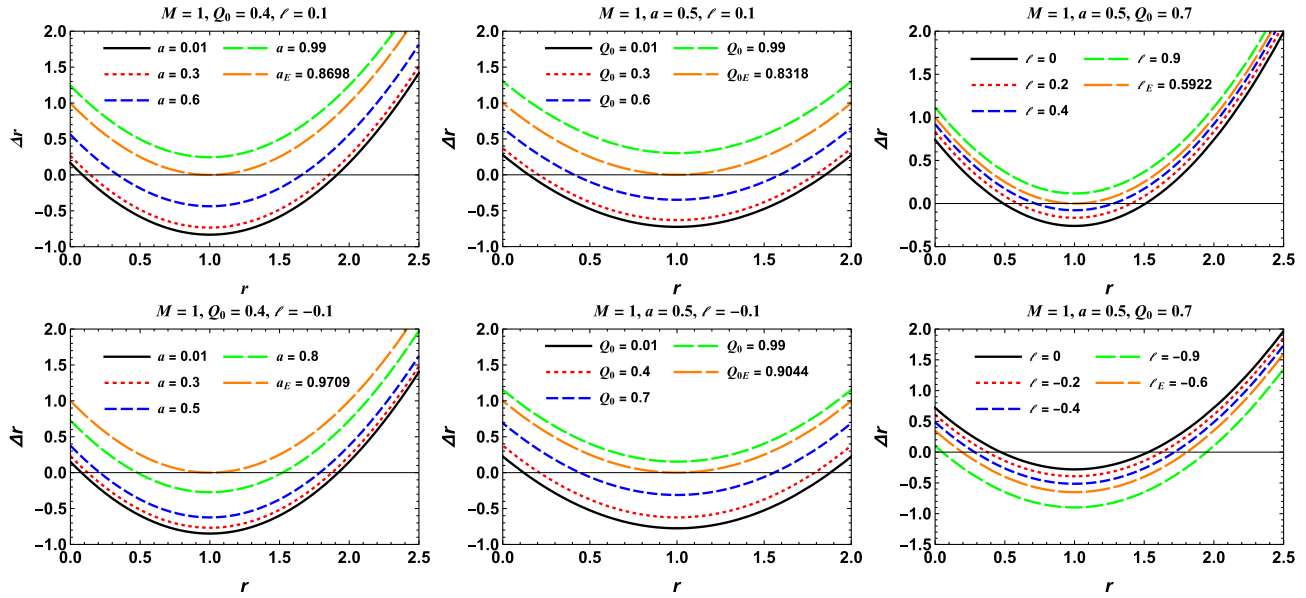


Fig. 2. (color online) Plots of the radial function $\Delta_r(r)$ as a function of r for different parameter combinations ($M = 1$). The columns, from left to right, show the effects of the spin a, charge Q_0, and Lorentz-violating parameter ℓ, while the upper and lower rows correspond to positive and negative ℓ, respectively. The roots of $\Delta_r(r) = 0$ represent the Cauchy horizon (left) and event horizon (right), and tangency indicates an extremal black hole.

$$H(x,p) = \frac{1}{2} g^{\mu\nu}(x) p_\mu p_\nu = 0, \tag{4}$$

where $g^{\mu\nu}$ denotes the inverse metric and p_μ is the photon's covariant four-momentum.

For a pressureless, non-magnetized plasma, the photon Hamiltonian must include a plasma-frequency term, which takes the form:

$$H(x,p) = \frac{1}{2}(g^{\mu\nu}(x) p_\mu p_\nu + \omega_p(x)^2) = 0, \tag{5}$$

where ω_p denotes the plasma electron frequency.

In general, an arbitrary spatial distribution of the plasma frequency tends to break the separability of the H-J equation. Previous studies [75, 90, 91] have indicated that variable separation requires the following condition:

$$\omega_p^2(r,\theta) = \frac{f_r(r) + f_\theta(\theta)}{r^2 + (1+\ell)a^2\cos^2\theta}, \tag{6}$$

where $f_r(r)$ and $f_\theta(\theta)$ are functions of their respective coordinates. This condition, first proposed by Perlick and Tsupko [65] for Kerr spacetime, has been widely adopted to study the shadows of axisymmetric black holes in plasma environments.

Given this separable structure, together with the stationarity and axisymmetry of the spacetime, the photon energy E and axial angular momentum L_z are conserved quantities, defined as: $E = -p_t$, $L_z = p_\phi$. Accordingly, we adopt the standard separable ansatz for the action S:

$$S = -Et + L_z\phi + S_r(r) + S_\theta(\theta), \tag{7}$$

where S_r and S_θ denote the radial and angular parts of the action, respectively. Substituting this expression into Eq. (5) allows us to separate the photon motion into independent radial and angular equations:

$$\left(\rho^2\frac{\partial S_r}{\partial r}\right)^2 = R(r), \quad \left(\rho^2\frac{\partial S_\theta}{\partial \theta}\right)^2 = \Theta(\theta). \tag{8}$$

The resulting separation constant is identified as the generalized Carter constant $\mathcal{K}$:

$$\begin{aligned}\mathcal{K} :=& -\frac{\Delta_r}{1+\ell}\left(\rho^2\frac{\partial S_r}{\partial r}\right)^2 + \frac{[(r^2+a^2(1+\ell))E - a\sqrt{1+\ell}L_z]^2}{\Delta_r} \\ &- (L_z - a\sqrt{1+\ell}E)^2 - f_r(r) = \left(\rho^2\frac{\partial S_\theta}{\partial\theta}\right)^2 \\ &- \left[a^2(1+\ell)E^2 - \frac{L_z^2}{\sin^2\theta}\right]\cos^2\theta + f_\theta(\theta).\end{aligned} \tag{9}$$

The radial potential $R(r)$ and angular potential $\Theta(\theta)$ for a photon are defined as follows:

$$\begin{aligned}\frac{\Delta_r}{1+\ell}\rho^2\dot{r}^2 =& \frac{\Delta_r}{1+\ell}R(r) = \frac{\left[(r^2+a^2(1+\ell))E - a\sqrt{1+\ell}L_z\right]^2}{\Delta_r} \\ &- (L_z - a\sqrt{1+\ell}E)^2 - \mathcal{K} - f_r(r), \\ \rho^2\dot{\theta}^2 =& \Theta(\theta) = \mathcal{K} + \left[a^2(1+\ell)E^2 - \frac{L_z^2}{\sin^2\theta}\right]\cos^2\theta - f_\theta(\theta).\end{aligned} \tag{10}$$

Shapiro's study [92] of the accretion environment of Kerr black holes indicates that, over a substantial radial range, the plasma density and the associated plasma frequency follow a power-law distribution: $\rho \propto \omega_p^2 \propto r^{-3/2}$.

Combining this astrophysical motivation with the separability condition in Eq. (6), we adopt the following plasma model [75]:

$$f_r(r) = \omega_c^2 \sqrt{r}, \quad f_\theta(\theta) = 0, \tag{11}$$

where ω_c is a constant. Substituting this model into the radial potential function in Eq. (10) yields a dimensionless coupling factor:

$$k \equiv \frac{\omega_c^2}{\omega_0^2}. \tag{12}$$

Here ω_0 denotes the photon frequency measured by an observer at infinity, and k is a parameter characterizing the plasma intensity.

Substituting the plasma model into Eq. (10), we obtain explicit expressions for the radial and angular effective potentials, $R(r)$ and $\Theta(\theta)$, respectively:

$$\begin{aligned}\frac{\Delta_r}{1+\ell}\rho^2\dot{r}^2 &= \frac{\Delta_r}{1+\ell}R(r) = \frac{[(r^2+a^2(1+\ell))E - a\sqrt{1+\ell}L_z]^2}{\Delta_r} \\ &\quad - (L_z - a\sqrt{1+\ell}E)^2 - \mathcal{K} - \omega_c^2\sqrt{r}, \rho^2\dot{\theta}^2 = \Theta(\theta) \\ &= \mathcal{K} + \left[a^2(1+\ell)E^2 - \frac{L_z^2}{\sin^2\theta}\right]\cos^2\theta. \end{aligned} \tag{13}$$

To establish the connection between the photon's orbit and the shadow observed by a distant observer, it is necessary to write the explicit geodesic equation for the photon. From Hamilton's canonical equations

$$\dot{x}^\mu = \frac{\partial H}{\partial p_\mu}, \quad \dot{p}_\mu = -\frac{\partial H}{\partial x^\mu}. \tag{14}$$

The first-order geodesic equations for photons are given by the following:

$$\begin{aligned}\rho^2\dot{t} &= \frac{a\sqrt{1+\ell}L_z[\Delta_r - (r^2+a^2(1+\ell))]}{\Delta_r} \\ &\quad + \frac{(r^2+a^2(1+\ell))^2E}{\Delta_r} - a^2(1+\ell)E\sin^2\theta, \\ \rho^2\dot{r} &= \sqrt{R(r)}, \\ \rho^2\dot{\theta} &= \sqrt{\Theta(\theta)}, \\ \rho^2\dot{\phi} &= \frac{a\sqrt{1+\ell}E[(r^2+a^2(1+\ell)) - \Delta_r]}{\Delta_r} \\ &\quad + \frac{L_z(\Delta_r - a^2(1+\ell)\sin^2\theta)}{\Delta_r\sin^2\theta}. \end{aligned} \tag{15}$$

Next, two dimensionless impact parameters are introduced:

$$\xi = \frac{L_z}{E}, \quad \eta = \frac{\mathcal{K}}{E^2}, \tag{16}$$

which correspond to the angular momentum normalized by the energy and the generalized Carter constant normalized by the energy, respectively.

The boundary of the black hole shadow is determined by unstable spherical photon orbits. The radial motion of these orbits satisfies the following critical conditions:

$$R(r) = 0, \quad R(r)' = 0 \tag{17}$$

and

$$\Theta(\theta) \geq 0 \quad \text{as} \quad \theta \in [0,\pi]. \tag{18}$$

By solving these conditions simultaneously, we obtain explicit expressions for the impact parameters ξ and η:

$$\begin{aligned}\xi &= \frac{r^2+a^2(1+\ell)}{a\sqrt{1+\ell}} \\ &\quad - \frac{\Delta_r}{a\sqrt{1+\ell}\Delta_r'}\left(2r + \sqrt{4r^2 - \frac{1}{2}\Delta_r' k r^{-1/2}}\right), \end{aligned} \tag{19}$$

$$\begin{aligned}\eta &= \frac{\Delta_r}{(\Delta_r')^2}\left(2r + \sqrt{4r^2 - \frac{1}{2}\Delta_r' k r^{-1/2}}\right)^2 \\ &\quad - \frac{1}{a^2(1+\ell)}\left[r^2 - \frac{\Delta_r}{\Delta_r'}\left(2r + \sqrt{4r^2 - \frac{1}{2}\Delta_r' k r^{-1/2}}\right)\right]^2 \\ &\quad - k\sqrt{r}. \end{aligned} \tag{20}$$

Substituting Eqs. (19) and (20) into Eq. (18), we obtain the existence condition for the photon region:

$$(\Delta_r X - \rho^2\Delta_r')^2 \leq a^2(1+\ell)\sin^2\theta\left[\Delta_r X^2 - k\sqrt{r}(\Delta_r')^2\right], \tag{21}$$

where

$$X = 2r + \sqrt{4r^2 - \frac{1}{2}\Delta_r' k r^{-1/2}}. \tag{22}$$

Unstable spherical null geodesics correspond to the boundary of the black hole shadow. Therefore, the stability of photon motion against radial perturbations at $r = r_p$ must be analyzed. This stability is determined by the sign of the second derivative of the effective potential $R(r)$. Using the previously derived Eqs. (13), (19), and (20), we obtain

$$\frac{R''(r)}{E^2}(\Delta_r')^2 = 4\Delta_r\Delta_r' X + 8r^2(\Delta_r')^2 - \Delta_r\Delta_r'' X^2 - \frac{k(\Delta_r')^2}{4r^{3/2}}(4r\Delta_r' - \Delta_r). \tag{23}$$

For the vacuum case $k=0$, with $X=4r$, the formula reduces to

$$\frac{R''(r)}{8E^2}(\Delta_r')^2 = 2r\Delta_r\Delta_r' + r^2(\Delta_r')^2 - 2r^2\Delta_r\Delta_r''. \tag{24}$$

The condition $R''(r_p)>0$ indicates an unstable spherical null geodesic, whereas $R''(r_p)<0$ implies a stable one.

The photon regions of the KN-like black hole in Bumblebee gravity surrounded by plasma are plotted in the (r,θ) plane, as shown in Figs. 3 and 4, where the orange region represents unstable photon orbits and the yellow region represents stable photon orbits. According to Refs. [69, 71, 93], we adopt two different scales along the r-direction to depict the entire spacetime, with particular emphasis on the exterior region $r>0$. Specifically, the radial coordinate is scaled as $r+M$ in the region $r>0$ and as $M\exp(r/M)$ in the region $r<0$. In this mapped space, the black hole throat at $r=0$ is indicated by a black dashed circle, while the blue ($\Delta_r \le 0$) and gray ($g_{tt}>0$) regions correspond to the event horizon and the ergosphere, respectively.

In Fig. 3, we fix $a=0.8$, $Q_0=0.5$, and $\ell=0.1$ to investigate the effect of the plasma parameter k on the photon regions. We clearly see an exterior photon region outside the outer horizon. Meanwhile, unstable and stable photon orbits may also appear in the interior photon region inside the inner horizon, where they are symmetric with respect to the equatorial plane. As k increases, the exterior photon region remains almost unchanged, whereas the interior photon region gradually diminishes until it vanishes completely.

It is crucial to clarify the physical distinction between the exterior and interior photon regions. As shown in Fig. 3, the interior photon regions are localized within the Cauchy horizon ($r<r_-$). Due to the causal structure of the spacetime, any photons trapped in or originating from these interior regions are confined within the event horizon and cannot reach a distant observer. Therefore, the interior photon regions have no practical relevance for the observable shadow or for astrophysical emission. The ob-

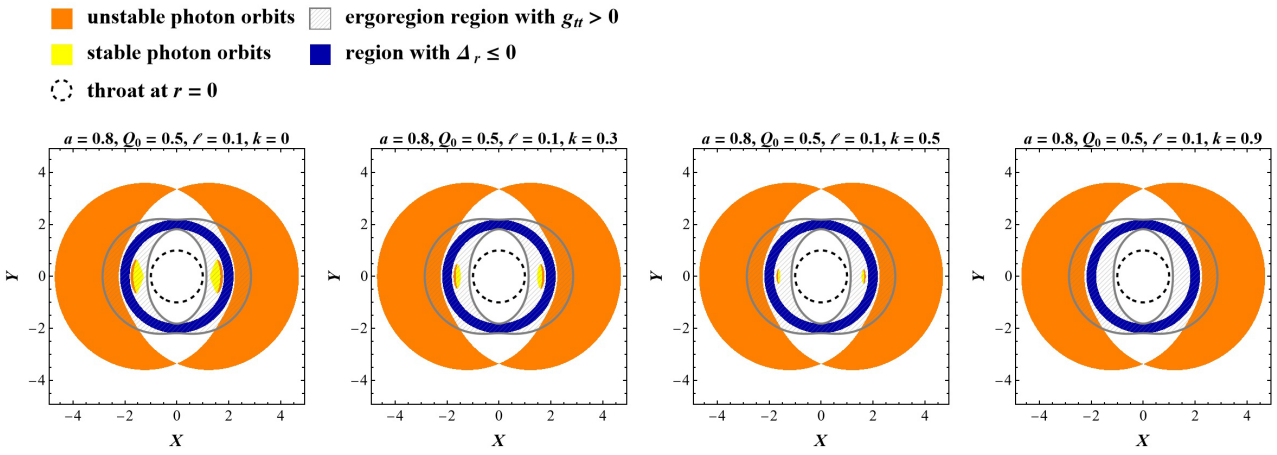


Fig. 3. (color online) Photon regions of the KN-like black hole in Bumblebee gravity surrounded by plasma in the (r,θ) plane. The parameters are set to $a=0.8$, $Q_0=0.5$, and $\ell=0.1$, with the plasma parameter k varied.

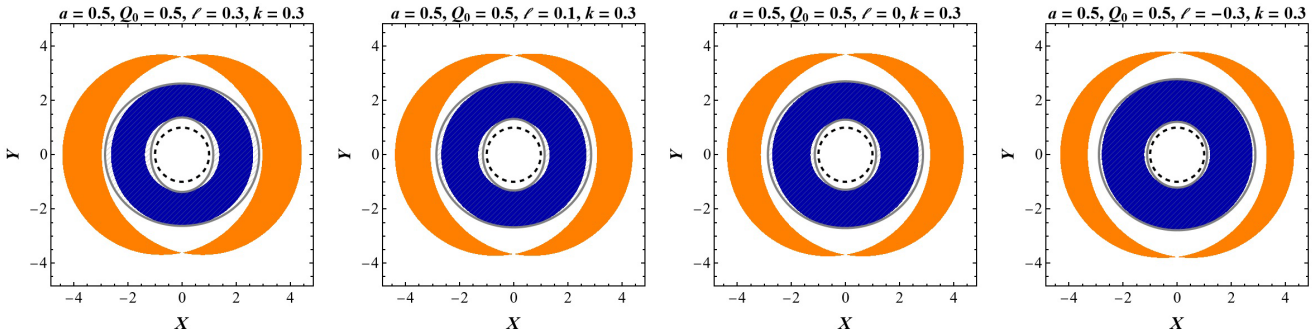


Fig. 4. (color online) Photon regions of the KN-like black hole in Bumblebee gravity surrounded by plasma in the (r,θ) plane. The parameters are set to $a=0.5$, $Q_0=0.5$, and $k=0.3$, with the Lorentz-violating parameter ℓ varied.

servable shadow boundary is determined by the unstable spherical photon orbits in the exterior photon region ($r > r_+$).

Figure 4 illustrates the influence of the Lorentz-violating parameter ℓ on the photon regions, with the background parameters fixed at $a = 0.5$, $Q_0 = 0.5$, and $k = 0.3$. As ℓ decreases, the exterior unstable photon region (orange area) shrinks. Furthermore, the blue region representing the event horizon expands, while the gray region representing the ergosphere closely follows the exterior of the horizon.

For an observer positioned at infinity $r_0 \to \infty$ with an inclination angle θ_0, we introduce the celestial coordinates (α,β). The mapping relation between these coordinates and the impact parameters (ξ,η) is given by

$$\alpha = -\frac{\xi}{\sin\theta_0}, \tag{25}$$

$$\beta = \pm\sqrt{\eta + a^2(1+\ell)\cos^2\theta_0 - \xi^2\cot^2\theta_0}. \tag{26}$$

Consequently, by parameterizing the unstable spherical photon orbits with the radius r_p, this mapping defines a closed curve on the observer's sky, which corresponds to the shadow of the Bumblebee black hole surrounded by plasma. Before proceeding with the shadow calculation, we first verify whether the radial function $\Delta(r) = 0$ admits real positive roots for each set of model parameters. This step ensures that the corresponding spacetime contains an event horizon. Parameter sets that do not satisfy the event-horizon condition are excluded directly from the calculation.

IV. THE BLACK HOLE SHADOW AND SHADOW OBSERVABLES

The shadow of the KN-like black hole in Bumblebee gravity surrounded by plasma is governed by the combined influence of the plasma parameter k and the Lorentz-violating parameter ℓ. In this section, we analyze the independent effects of these parameters on the shadow and its observables. Subsequently, we briefly discuss the energy emission rate.

To understand the independent influence of each physical parameter on the shadow, we examine the response to variations in a single parameter while keeping the others fixed, as illustrated in Fig. 5. The results indicate two main trends. First, increasing the spin parameter a or the Lorentz-violating parameter ℓ primarily enhances the left-right asymmetry of the shadow relative to the $\alpha = 0$ axis, resulting in greater distortion. Second, increasing the charge parameter Q_0 or the plasma parameter k predominantly reduces the shadow size.

Physically, the Lorentz symmetry-breaking effect modifies the spacetime structure. Together with the black hole's rotation, this deformation alters the photon trajectories, specifically leading to an increasingly asymmetric separation between the prograde and retrograde unstable photon orbits. Consequently, this coupling-induced asymmetry enhances the distortion of the shadow.

Because these parameters significantly affect the shadow's shape and size, it is necessary to introduce a set of observables that can accurately characterize the geometry of the black hole shadow.

Following the reference circle method proposed by Hioki and Maeda [94], we quantify the shadow size and shape, as illustrated in Fig. 6. By constructing a reference circle passing through three characteristic points—the top (T), bottom (B), and rightmost (R) points of the shadow boundary—we define the equivalent shadow radius and the distortion parameter as follows [94]:

$$R_s = \frac{(\alpha_t-\alpha_r)^2+\beta_t^2}{2|\alpha_t-\alpha_r|}, \quad \delta_s = \frac{D_{cs}}{R_s} = \frac{|\alpha_L-\alpha_L'|}{R_s}. \tag{27}$$

Figure 7 shows the behavior of the shadow radius R_s and the distortion parameter δ_s as the physical parameters vary. The shadow radius R_s is primarily reduced by increasing the plasma parameter k and the charge parameter Q_0. It exhibits a slight decrease with the Lorentz-violating parameter ℓ, but remains almost unchanged with the spin parameter a. In contrast, the distortion parameter δ_s is significantly enhanced with increasing ℓ and a. Furthermore, while δ_s is practically insensitive to k, it increases slightly for larger values of Q_0.

However, the Hioki-Maeda observables R_s and δ_s have inherent limitations: they are based on the assumption of approximate symmetry and typically presume an equatorial viewing angle ($\theta_0 = \pi/2$). Thus, these geometric requirements make them less effective for characterizing highly irregular or distorted shadow shapes. To overcome these limitations and characterize shadow geometries with more general shapes, we further introduce two coordinate-independent observables proposed by Kumar and Ghosh [95], which do not rely on strict symmetry assumptions: the shadow area A and the oblateness D, defined as:

$$A = 2\int\beta(r_p)\mathrm{d}\alpha(r_p) = 2\int_{r_p^{\min}}^{r_p^{\max}}\left(\beta(r_p)\frac{\mathrm{d}\alpha(r_p)}{\mathrm{d}r_p}\right)\mathrm{d}r_p,$$
$$D = \frac{\alpha_r-\alpha_l}{\beta_t-\beta_b}. \tag{28}$$

Here, $r_p^{\min}$ and $r_p^{\max}$ denote the radii of the prograde and retrograde photon orbits, determined by $\eta(r_p) = 0$. For an observer in the equatorial plane, the oblateness D [96] lies in the interval $[\sqrt{3}/2, 1]$. The upper limit, $D = 1$, corresponds to the spherically symmetric Schwarzschild lim-

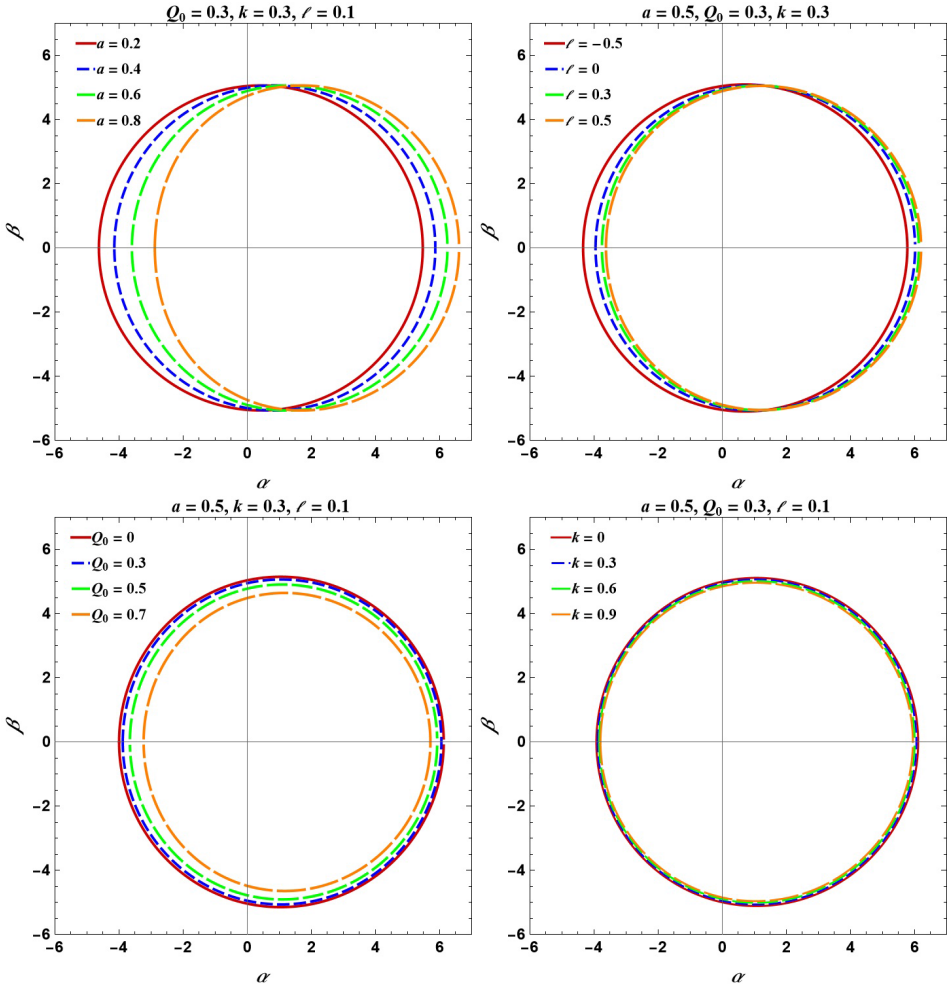


Fig. 5. (color online) Shadows of the KN-like black hole in Bumblebee gravity surrounded by plasma, illustrating the independent effects of variations in the parameters a, ℓ, Q_0, and k.

it, whereas the lower bound, $D = \sqrt{3}/2$, characterizes the extremal Kerr black hole.

From an observational perspective, these two sets of observables serve distinct purposes. The Hioki-Maeda parameters R_s and δ_s are theoretical diagnostics for weakly distorted shadows under idealized conditions. In contrast, the shadow area A and oblateness D are more robust against observational uncertainties. Specifically, A effectively captures the total shadow size through global integration, while D provides a universal measure of asymmetry.

Figure 8 illustrates the variation trends of the shadow area A and the oblateness D under different physical parameters. As shown in the upper panels, increasing the Lorentz-violating parameter ℓ reduces both the shadow area A and the oblateness D. Moreover, as the plasma parameter k increases, the shadow area decreases significantly, whereas the oblateness increases slightly. Conversely, the lower panels show the influence of the spin parameter a and the charge parameter Q_0. As the spin parameter a increases, the oblateness D decreases sharply, and the shadow area A decreases slightly. Furthermore, increasing the charge parameter Q_0 leads to a significant decrease in the shadow area and a reduction in the oblateness.

In addition to the geometric shadow properties, the high-frequency energy emission rate of a black hole in the geometric optics limit can also reflect the spacetime structure. As a complement to the shadow analysis above, we further investigate the high-frequency emission rate of the KN-like black hole in a plasma background. For an observer at infinity, the high-frequency energy emission rate of the black hole can be expressed as:

$$\frac{\mathrm{d}^2 E(\omega)}{\mathrm{d}\omega\,\mathrm{d}t} = \frac{2\pi^2 \sigma_{\lim}}{\mathrm{e}^{\omega/T_{\mathrm{H}}} - 1}\omega^3. \tag{29}$$

Here, ω is the photon frequency, and T_{H} is the Hawking temperature. $\sigma_{\lim}$ denotes the high-frequency absorption cross-section. In the geometric-optics limit, it approaches a constant value, which corresponds to the geometric shadow area of the black hole [97]:

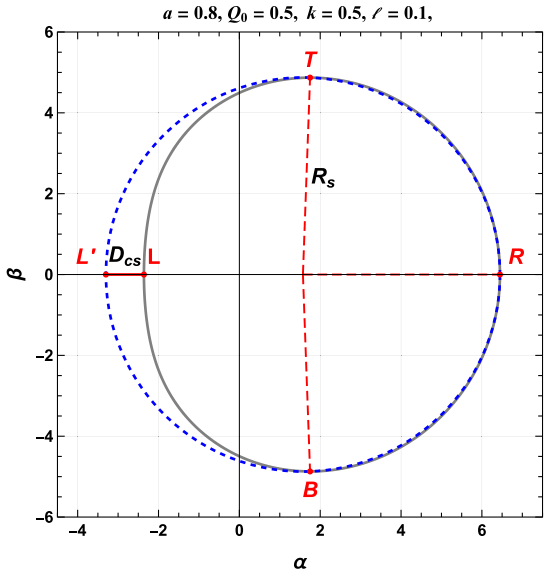


Fig. 6. (color online) Illustration of the shadow observables defined by the reference circle method. The solid black curve represents the black hole shadow, and the dashed blue curve denotes the reference circle. This circle is constructed to pass through three characteristic points: the top (T), bottom (B), and rightmost (R) points of the shadow. Here, L and L' denote the left endpoints of the shadow and the reference circle, respectively. The parameter D_{cs} is defined as $D_{cs} \equiv \alpha_{L'} - \alpha_L$.

$$\sigma_{\rm lim} \approx \pi R_s^2, \tag{30}$$

where R_s is the black hole shadow radius obtained above.

The Hawking temperature $T_{\rm H}$ in the KN-like black hole background is given by:

$$T_{\rm H} = \frac{r_+ - M}{2\pi\left(r_+^2 + a^2(1+\ell)\right)}. \tag{31}$$

Figure 9 displays the response of the energy emission rate to various parameters while the others are held fixed. The plots in the upper row show that the peak of the energy emission rate decreases significantly as a or Q_0 increases, and the peak shifts to a lower-frequency region. In contrast, the plots in the bottom row show that, although increasing k or ℓ also suppresses the energy emission rate, the reduction is relatively mild.

V. CONSTRAINTS FROM EHT OBSERVATIONS ON M87*

The shadow image of the supermassive black hole M87* captured by the EHT collaboration reveals a distinct crescent-shaped emission ring structure. In particular, based on the estimated inclination angle for the M87* observation, $\theta_0 = 17^\circ$, the EHT collaboration extracted key geometric constraints from this image [1, 4, 5], including the circularity deviation $\Delta C \lesssim 0.1$, axis ratio $1 < D_x \lesssim \frac{4}{3}$, and angular diameter $\theta_d = 42 \pm 3\,\mu$as.

In this section, we consider the M87* black hole as a Kerr-Newman-like (KN-like) black hole surrounded by plasma within the framework of Bumblebee gravity. We then use the aforementioned EHT observational constraints to restrict the model parameters, thereby identifying the physically feasible regions of the model.

In the celestial observer's plane, the shadow can be represented in polar coordinates $(R(\varphi),\varphi)$, with the origin at the shadow center (α_C,β_C). Next, we present the expressions for ΔC, D_x, and θ_d. First, define the shadow center point:

$$\beta_C = 0, \quad \alpha_C = \frac{\alpha_R + \alpha_L}{2}, \tag{32}$$

where α_R and α_L denote the α coordinates of the right and left edges of the shadow, respectively. Next, we represent the shadow boundary in polar coordinates:

$$\begin{aligned} R(\varphi) &= \sqrt{(\alpha-\alpha_C)^2 + (\beta-\beta_C)^2}, \\ \varphi &= \tan^{-1}\left(\frac{\beta}{\alpha-\alpha_C}\right). \end{aligned} \tag{33}$$

Define the average radius [98] as:

$$\bar{R}^2 = \frac{1}{2\pi}\int_0^{2\pi} R^2(\varphi)\,{\rm d}\varphi. \tag{34}$$

The circularity deviation is then defined as [99]:

$$\Delta C = \frac{1}{\bar{R}}\sqrt{\frac{1}{2\pi}\int_0^{2\pi}(R(\varphi)-\bar{R})^2\,{\rm d}\varphi}. \tag{35}$$

The axial ratio is defined as the ratio of the shadow's vertical diameter to its horizontal diameter [100]:

$$D_x = \frac{\beta_t - \beta_b}{\alpha_r - \alpha_l}. \tag{36}$$

The angular diameter is given by the following formula [101]:

$$\theta_d = \frac{2R_a}{d}, \quad R_a = \sqrt{\frac{A}{\pi}}, \tag{37}$$

where d is the distance from Earth to M87*, R_a is the shadow areal radius, and A is the shadow area.

Next, we model the supermassive black hole M87* as a KN-like black hole within the framework of Bumblebee gravity, immersed in a non-homogeneous power-law plasma. By setting the mass $M = 6.5\times10^9 M_\odot$ and the dis-

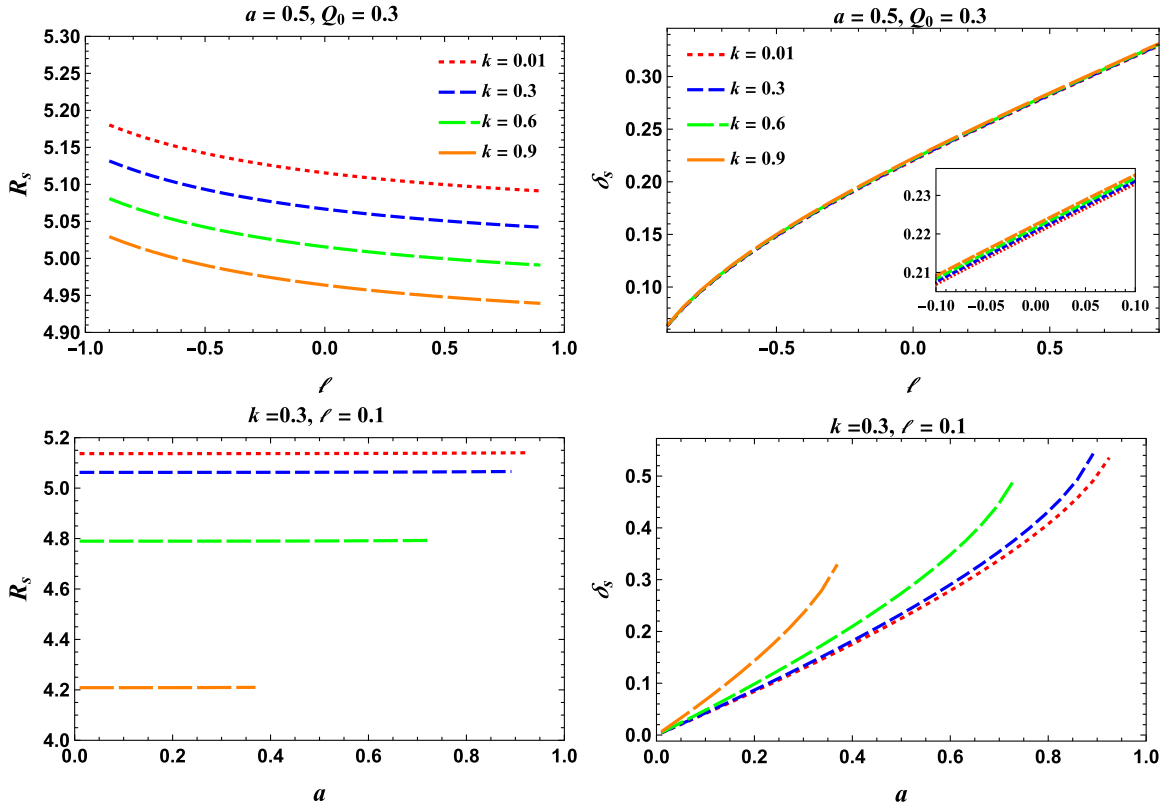


Fig. 7. (color online) Variations in the shadow radius R_s and the distortion parameter δ_s for a KN-like black hole in Bumblebee gravity surrounded by plasma. The fixed parameters are $a = 0.5$, $Q_0 = 0.3$ in the upper row and $k = 0.3$, $\ell = 0.1$ in the bottom row.

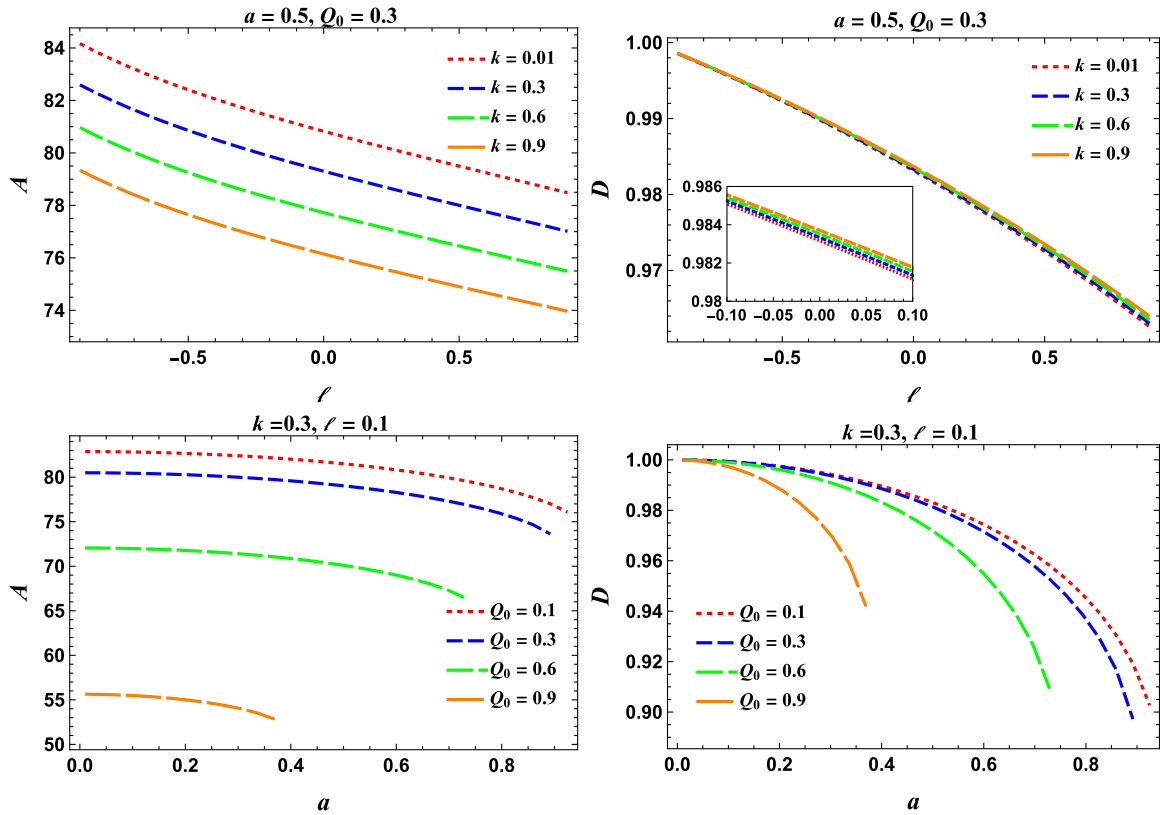


Fig. 8. (color online) Variations of the shadow area A and the oblateness D for a KN-like black hole in Bumblebee gravity surrounded by plasma. The fixed parameters are set to $a = 0.5$, $Q_0 = 0.3$ (upper row), and $k = 0.3$, $\ell = 0.1$ (bottom row).

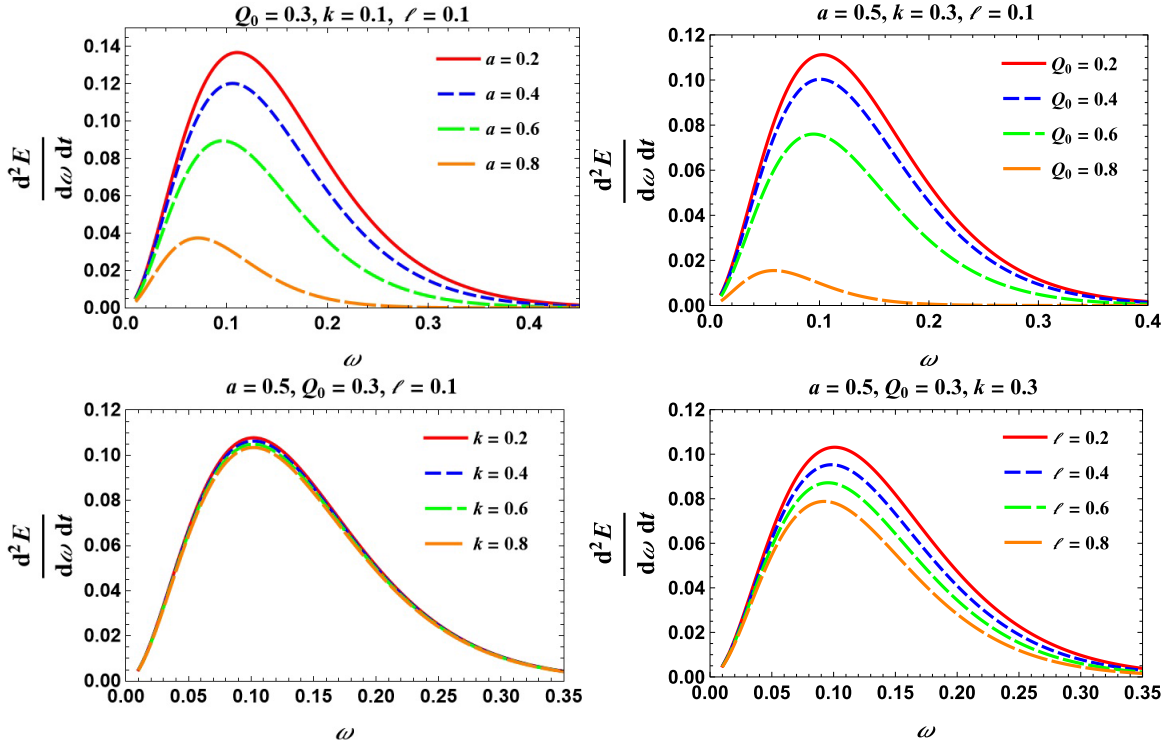


Fig. 9. (color online) High-frequency energy emission rate as a function of frequency ω for different values of the physical parameters (a, Q_0, k, ℓ).

tance $d = 16.8\,\mathrm{Mpc}$, we can determine the theoretical observables of our model. Furthermore, we adopt an inclination angle of $\theta_0 = 17^\circ$ for M87*, which is estimated based on the orientation of the relativistic jet [102].

Figure 10 compares the theoretical shadow predictions of our black hole model with the EHT observational constraints for M87* at $\theta_0 = 17^\circ$ in the (a, Q_0) parameter plane. The two solid black curves represent the constant angular diameters $\theta_d = 39\,\mu\mathrm{as}$ and $\theta_d = 45\,\mu\mathrm{as}$, respectively. The region between them denotes the parameter space consistent with the EHT constraints. More specifically, when $k = 0.3$ and $\ell = 0.1$, the EHT observation $\theta_d = 42 \pm 3\,\mu\mathrm{as}$ excludes part of the parameter space, including regions corresponding to low spin and charge $(a < 0.06, Q_0 < 0.04)$ and to high charge $Q_0 > 0.77$. By contrast, the EHT observational constraints on the circularity deviation $\Delta C \lesssim 0.1$ and axis ratio $1 < D_x \lesssim 4/3$ are satisfied throughout all considered parameter regions, which implies that the circularity deviation and axis ratio alone are insufficient to constrain the parameters of the KN-like black hole.

The density plots in the (ℓ, k) parameter plane are presented in Fig. 11 for $a = 0.5$ and $Q_0 = 0.3$. On the one hand, all parameter regions satisfy the constraints

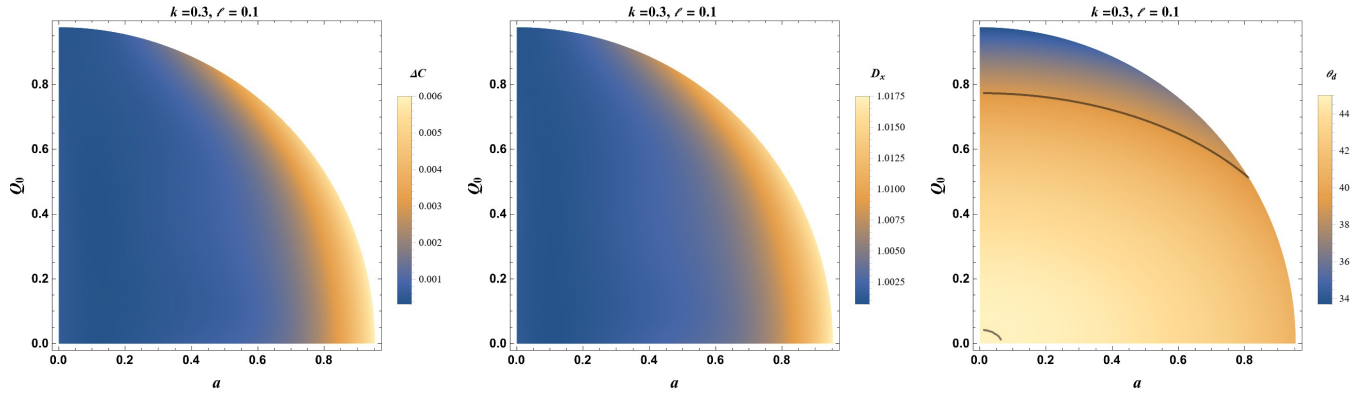


Fig. 10. (color online) Density plots of the circular deviation ΔC, axial ratio D_x, and angular diameter θ_d in the (a, Q_0) parameter plane for $\theta_0 = 17^\circ$. The parameter plane includes only values for which an event horizon exists.

$\Delta C \lesssim 0.1$ and $1 < D_x \lesssim 4/3$, indicating consistency with the EHT observations. On the other hand, the solid black curve corresponds to the angular diameter $\theta_d = 45\,\mu$as in the density plot. The region with $0 < k < 0.3$ and $-1 < \ell < -0.85$ is therefore excluded by the EHT angular diameter constraint.

It should be emphasized that the aforementioned parameter constraints are highly contingent upon our specific astrophysical assumptions, including the assumed inclination angle ($\theta_0 = 17°$), the estimated black hole mass and distance, and the chosen non-homogeneous plasma model. Therefore, it is important to clarify that our results do not definitively "verify" Bumblebee gravity, but rather demonstrate that certain parameter ranges within this framework are consistent with the current EHT constraints. In other words, within the allowed parameter space, current EHT observations are insufficient to rule out Bumblebee gravity as a viable effective framework.

Therefore, we conclude that EHT observations of the M87* black hole shadow cannot rule out the existence of a KN-like black hole in Bumblebee gravity surrounded by plasma. To further constrain the spin parameter a and the Lorentz-violating parameter ℓ, the 1σ and 2σ confidence intervals are plotted based on the aforementioned angular diameter density maps. Figure 12 shows that the adopted mass $M = 6.5\times10^9 M_\odot$ falls within the 1σ band, indicating that our setup is consistent with the EHT constraints. For $Q_0 = 0.3$, $k = 0.3$, $\ell = 0.1$, the 1σ bound on mass is $5.72\times10^9 M_\odot < M < 7.18\times10^9 M_\odot$, and the 2σ bound is $5.29\times10^9 M_\odot < M < 7.66\times10^9 M_\odot$; while for $a = 0.5$, $Q_0 = 0.3$, $k = 0.3$, the 1σ bound on mass is $5.62\times10^9 M_\odot < M < 6.94\times10^9 M_\odot$, and the 2σ bound is $5.20\times10^9 M_\odot < M < 7.41\times10^9 M_\odot$.

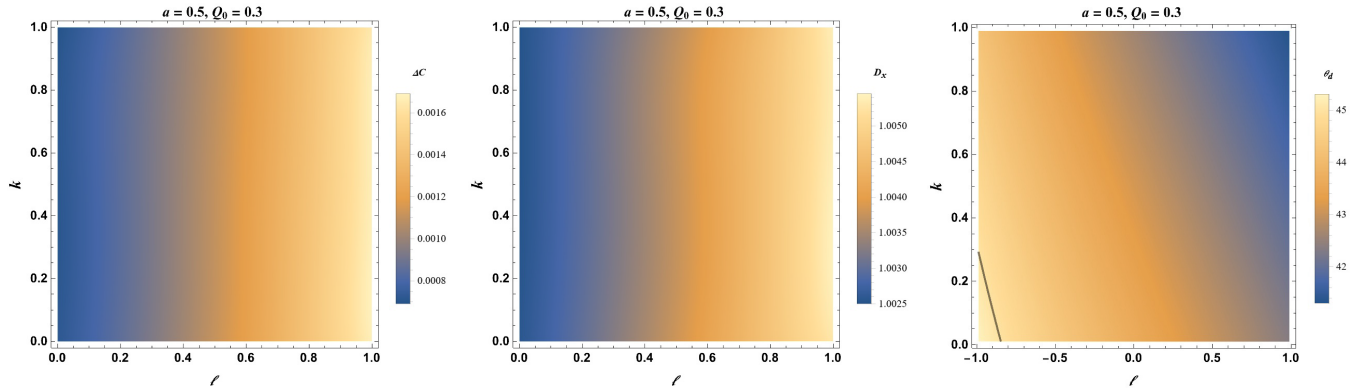


Fig. 11. (color online) Density plots of the circular deviation ΔC, axial ratio D_x, and angular diameter θ_d in the (ℓ, k) parameter plane for $\theta_0 = 17°$. The parameter plane includes only parameter values for which an event horizon exists.

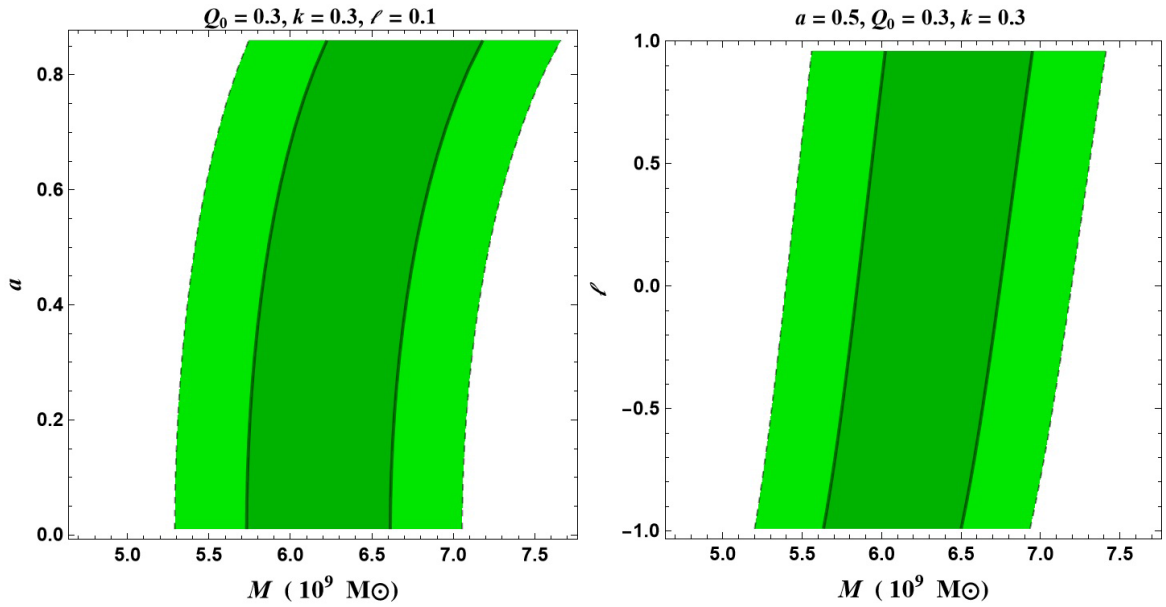


Fig. 12. (color online) Constraints on the parameter a, ℓ, and the estimated M87* black hole mass $M(\times10^9 M_\odot)$ obtained using the M87* shadow angular size within 1σ (dark green region) and 2σ (light green region).

VI. CONCLUSION

To summarize, in this work, we investigated the shadow of a charged rotating black hole within the framework of Bumblebee gravity, immersed in a non-homogeneous power-law plasma model. To analyze the shadow characteristics under the combined effects of Lorentz symmetry breaking (LSB) and the plasma medium, we studied the black hole shadow and its associated observables. Furthermore, we used the latest EHT observations to constrain the model parameters.

First, we examined the influence of the Lorentz-violating parameter ℓ and the charge parameter Q_0 on the event horizon through an analysis of the parameter space and spacetime structure. As shown in Fig. 1, as ℓ and Q_0 increase, the allowed range of the spin parameter a is significantly reduced, and the spacetime structure shows a strong tendency toward an extremal black hole. This fundamental geometric analysis not only established the physical bounds for subsequent simulations but also indicates that LSB provides a non-trivial correction to the properties of the strong gravitational field.

Building on this, we derived the null geodesic equations for photons in a plasma model using the separable Hamilton-Jacobi equation. Along with the analysis of the photon regions, we numerically calculated the black hole shadow. By systematically comparing the effects of the individual parameters on the shadow and its observables, we categorized the roles of the four physical parameters into two distinct physical effects: the spin a and the Lorentz-violating parameter ℓ mainly produce a left-right asymmetry in the shadow relative to the $\alpha = 0$ axis, thereby dominating the drag distortion of the shadow, whereas the charge parameter Q_0 and the plasma parameter k dominate the radial contraction of the shadow size.

Finally, we mapped three key observables of the M87* black hole — the angular diameter, axial ratio, and circularity deviation — onto our theoretical model. Figs. 10 and 11 demonstrate that, although the current observational precision is insufficient to completely rule out the Bumblebee gravity model, we successfully excluded part of the parameter space characterized by low values of the Lorentz-violating parameter and low plasma density. As shown in Fig. 12, the confidence interval analysis demonstrates that our proposed model is self-consistent under the EHT constraints. While this result does not definitively verify Bumblebee gravity, it demonstrates the feasibility of using black hole images to constrain fundamental physics under specific astrophysical priors (such as the assumed black hole mass, inclination angle, and plasma model). Consequently, it provides a theoretical reference for future, higher-precision gravitational tests.

Building on previous shadow studies, the main extensions of our work are reflected in three aspects. First, we provide a comprehensive analysis of the photon regions, distinguishing the observational relevance of the interior and exterior orbits. Second, by analyzing the shadow observables, we identify two distinct physical effects among the parameters: the spin a and the Lorentz-violating parameter ℓ dominate the shadow distortion, whereas the charge Q_0 and plasma parameter k govern its radial shrinkage. Finally, using two sets of observables, we constrain this coupled model with EHT observations of M87* by plotting the viable parameter spaces and their 1σ and 2σ confidence intervals, thereby evaluating its astrophysical feasibility.

Furthermore, it should be emphasized that our theoretical model relies on certain idealized analytical approximations. Specifically, the selected non-homogeneous power-law plasma profile should be regarded as an analytically tractable approximation rather than a highly realistic accretion-flow model. Although realistic accretion flows are undoubtedly more complex, the adopted plasma model provides a necessary and valuable theoretical baseline for evaluating plasma effects on the black hole shadow.

References

[1] K. Akiyama *et al.* (Event Horizon Telescope Collaboration), Astrophys. J. Lett. **875**, L1 (2019)
[2] K. Akiyama *et al.* (Event Horizon Telescope Collaboration), Astrophys. J. Lett. **875**, L2 (2019)
[3] K. Akiyama *et al.* (Event Horizon Telescope Collaboration), Astrophys. J. Lett. **875**, L3 (2019)
[4] K. Akiyama *et al.* (Event Horizon Telescope Collaboration), Astrophys. J. Lett. **875**, L4 (2019)
[5] K. Akiyama *et al.* (Event Horizon Telescope Collaboration), Astrophys. J. Lett. **875**, L5 (2019)
[6] K. Akiyama *et al.* (Event Horizon Telescope Collaboration), Astrophys. J. Lett. **875**, L6 (2019)
[7] K. Akiyama *et al.* (Event Horizon Telescope Collaboration), Astrophys. J. Lett. **930**, L12 (2022)
[8] K. Akiyama *et al.* (Event Horizon Telescope Collaboration), Astrophys. J. Lett. **930**, L13 (2022)
[9] K. Akiyama *et al.* (Event Horizon Telescope Collaboration), Astrophys. J. Lett. **930**, L14 (2022)
[10] D. Psaltis, Gen. Rel. Grav. **51**, 137 (2019)
[11] K. Glampedakis and G. Pappas, Phys. Rev. D **104**, L081503 (2021)
[12] F. H. Vincent, M. Wielgus, M. A. Abramowicz *et al.*, Astron. Astrophys. **646**, A37 (2201)
[13] S. Vagnozzi, R. Roy, Y. D. Tsai *et al.*, Class. Quant. Grav. **40**, 165007 (2023)
[14] L. Hui, Ann. Rev. Astron. Astrophys. **59**, 247 (2021)
[15] J. Antoniadis *et al.* (EPTA and InPTA Collaboration), Astron. Astrophys. **685**, A94 (2024)
[16] A. Afzal *et al.* (NANOGrav Collaboration), Astrophys. J. Lett. **951**, L11 (2023)
[17] T. Clifton, P. G. Ferreira, A. Padilla *et al.*, Phys. Rept. **513**,

1 (2012)
[18] P. G. S. Fernandes, P. Carrilho, T. Clifton *et al.*, Class. Quant. Grav. **39**, 063001 (2022)
[19] S. Shankaranarayanan and J. P. Johnson, Gen. Rel. Grav. **54**, 44 (2022)
[20] M. Han and H. Liu, Class. Quant. Grav. **39**, 035011 (2022)
[21] C. Zhang, Y. Ma, and J. Yang, Phys. Rev. D **108**, 104004 (2023)
[22] R. A. Konoplya, Phys. Lett. B **804**, 135363 (2020)
[23] A. Uniyal, R. C. Pantig, and A. Övgün, Phys. Dark Univ. **40**, 101178 (2023)
[24] H. O. Silva, A. Ghosh, and A. Buonanno, Phys. Rev. D **107**, 044030 (2023)
[25] F. Atamurotov, I. Hussain, G. Mustafa *et al.*, Chin. Phys. C **47**, 025102 (2023)
[26] D. Ayzenberg and N. Yunes, Class. Quant. Grav. **35**, 235002 (2018)
[27] Z. L. Wang and E. Battista, Eur. Phys. J. C **85**, 304 (2025)
[28] X. M. Kuang, Z. Y. Tang, B. Wang *et al.*, Phys. Rev. D **106**, 064012 (2022)
[29] V. A. Kostelecky, Phys. Rev. D **69**, 105009 (2004)
[30] C. Ding, X. Chen, and X. Fu, Nucl. Phys. B **975**, 115688 (2022)
[31] M. Bin-Asfour, A. Fayyaz, G. Abbas *et al.*, Nucl. Phys. B **1024**, 117346 (2026)
[32] B. Eslam Panah, Phys. Lett. B **861**, 139273 (2025)
[33] R. Karmakar, D. J. Gogoi, and U. D. Goswami, Phys. Dark Univ. **41**, 101249 (2023)
[34] Y. Shi and A. A. Araújo Filho, JCAP **11**, 045 (2025)
[35] V. A. Kostelecky and S. Samuel, Phys. Rev. D **39**, 683 (1989)
[36] T. Jacobson, S. Liberati and D. Mattingly, Annals Phys. **321**, 150 (2006)
[37] V. A. Kostelecký and M. Mewes, Phys. Lett. B **757**, 510 (2016)
[38] D. Colladay and V. A. Kostelecky, Phys. Rev. D **58**, 116002 (1998)
[39] V. A. Kostelecky and S. Samuel, Phys. Rev. Lett. **63**, 224 (1989)
[40] A. V. Kostelecky and J. D. Tasson, Phys. Rev. D **83**, 016013 (2011)
[41] R. Casana, A. Cavalcante, F. P. Poulis *et al.*, Phys. Rev. D **97**, 104001 (2018)
[42] D. Liang, R. Xu, Z. F. Mai *et al.*, Phys. Rev. D **107**, 044053 (2023)
[43] A. Kumar, S. U. Islam, and S. G. Ghosh, Phys. Dark Univ. **52**, 102307 (2026)
[44] Q. Qi, Y. Sang, and X. M. Kuang, Sci. China Phys. Mech. Astron. **69**, 260414 (2026)
[45] İ. Güllü and A. Övgün, Annals Phys. **436**, 168721 (2022)
[46] Q. G. Bailey, H. S. Murray, and D. T. Walter-Cardona, Phys. Rev. D **112**, 024069 (2025)
[47] C. Ding, C. Liu, R. Casana *et al.*, Eur. Phys. J. C **80**, 178 (2020)
[48] C. Ding and X. Chen, Chin. Phys. C **45**, 025106 (2021)
[49] S. K. Jha and A. Rahaman, Eur. Phys. J. C **81**, 345 (2021)
[50] A. A. Araújo Filho, J. R. Nascimento, A. Y. Petrov *et al.*, JCAP **07**, 004 (2024)
[51] A. Uniyal, S. Kanzi, and İ. Sakallı, Eur. Phys. J. C **83**, 668 (2023)
[52] X. M. Kuang and A. Övgün, Annals Phys. **447**, 169147 (2022)
[53] R. C. Pantig, S. Kala, A. Övgün *et al.*, Int. J. Geom. Methods Mod. Phys. **22**, 2550240 (2025)
[54] S. U. Islam, S. G. Ghosh, and S. D. Maharaj, JCAP **12**, 047 (2024)
[55] X. J. Gao, Eur. Phys. J. C **84**, 973 (2024)
[56] Y. Sekhmani, S. K. Maurya, J. Rayimbaev *et al.*, Phys. Dark Univ. **50**, 102116 (2025)
[57] A. A. Araújo Filho, N. Heidari, I. P. Lobo *et al.*, Annals Phys. **490**, 170487 (2026)
[58] F. Yuan and R. Narayan, Ann. Rev. Astron. Astrophys. **52**, 529 (2014)
[59] V. Perlick, O. Y. Tsupko, and G. S. Bisnovatyi-Kogan, Phys. Rev. D **92**, 104031 (2015)
[60] G. S. Bisnovatyi-Kogan and O. Y. Tsupko, Mon. Not. Roy. Astron. Soc. **404**, 1790 (2010)
[61] M. Sárený and V. Balek, Gen. Rel. Grav. **51**, 141 (2019)
[62] F. Atamurotov and B. Ahmedov, Phys. Rev. D **92**, 084005 (2015)
[63] A. Abdujabbarov, M. Amir, B. Ahmedov *et al.*, Phys. Rev. D **93**, 104004 (2016)
[64] G. S. Bisnovatyi-Kogan, and O. Y. Tsupko, Universe **3**, 57 (2017)
[65] V. Perlick and O. Y. Tsupko, Phys. Rev. D **95**, 104003 (2017)
[66] Z. Zhang, H. Yan, M. Guo *et al.*, Phys. Rev. D **107**, 024027 (2023)
[67] A. Chowdhuri and A. Bhattacharyya, Phys. Rev. D **104**, 064039 (2021)
[68] Q. Li, Y. Zhu, and T. Wang, Eur. Phys. J. C **82**, 2 (2022)
[69] Q. Sun, Y. Zhang, C. H. Xie *et al.*, Phys. Dark Univ. **46**, 101599 (2024)
[70] K. Nozari, S. Saghafi, and A. Mohammadpour, Eur. Phys. J. C **84**, 778 (2024)
[71] Y. Meng, X. M. Kuang, and Z. Y. Tang, Phys. Rev. D **106**, 064006 (2022)
[72] M. Heydari-Fard, M. Heydari-Fard, and N. Riazi, Int. J. Mod. Phys. D **32**, 2350088 (2023)
[73] W. Liu, D. Wu, and J. Wang, JCAP **05**, 017 (2025)
[74] G. Z. Babar, A. Z. Babar, and F. Atamurotov, Eur. Phys. J. C **80**, 761 (2020)
[75] J. Badía and E. F. Eiroa, Phys. Rev. D **104**, 084055 (2021)
[76] Y. Hou, Z. Zhang, H. Yan *et al.*, Phys. Rev. D **106**, 064058 (2022)
[77] X. Wang, Y. Hou, X. Wan *et al.*, JCAP **02**, 050 (2026)
[78] S. Chen and J. Jing, Sci. China Phys. Mech. Astron. **67**, 250411 (2024)
[79] S. Chen and J. Jing, JCAP **05**, 023 (2024)
[80] F. Atamurotov, M. Jamil, and K. Jusufi, Chin. Phys. C **47**, 035106 (2023)
[81] N. U. Molla and U. Debnath, Annals Phys. **453**, 169304 (2023)
[82] Y. Pahlavon, F. Atamurotov, K. Jusufi *et al.*, Phys. Dark Univ. **45**, 101543 (2024)
[83] J. Badía and E. F. Eiroa, Phys. Rev. D **107**, 124028 (2023)
[84] R. Ali, M. Awais, and A. Mahmood, Annalen Phys. **535**, 2300236 (2023)
[85] H. M. Wang and S. W. Wei, Eur. Phys. J. Plus **137**, 571 (2022)
[86] R. M. Wald, Phys. Rev. D **10**, 1680 (1974)
[87] S. S. Komissarov, Mon. Not. Roy. Astron. Soc. **512**, 2798 (2022)
[88] P. Kocherlakota *et al.* (Event Horizon Telescope Collaboration), Phys. Rev. D **103**, 104047 (2021)
[89] J. Z. Liu, W. D. Guo, S. W. Wei *et al.*, Eur. Phys. J. C **85**,

145 (2025)
[90] B. Bezdekova, V. Perlick, and J. Bicak, J. Math. Phys. **63**, 092501 (2022)
[91] M. Fathi, M. Olivares, and J. R. Villanueva, Eur. Phys. J. C **81**, 987 (2021)
[92] S. L. Shapiro, Astrophys. J. **189**, 343 (1974)
[93] A. Grenzebach, V. Perlick, and C. Lämmerzahl, Phys. Rev. D **89**, 124004 (2014)
[94] K. Hioki and K. i. Maeda, Phys. Rev. D **80**, 024042 (2009)
[95] R. Kumar and S. G. Ghosh, Astrophys. J. **892**, 78 (2020)
[96] O. Y. Tsupko, Phys. Rev. D **95**, 104058 (2017)
[97] S. W. Wei and Y. X. Liu, JCAP **11**, 063 (2013)
[98] C. Bambi, K. Freese, S. Vagnozzi *et al*., Phys. Rev. D **100**, 044057 (2019)
[99] M. Afrin, R. Kumar, and S. G. Ghosh, Mon. Not. Roy. Astron. Soc. **504**, 5927 (2021)
[100] I. Banerjee, S. Chakraborty, and S. SenGupta, Phys. Rev. D **101**, 041301 (2020)
[101] R. Kumar and S. G. Ghosh, JCAP **07**, 053 (2020)
[102] R. Craig Walker, P. E. Hardee, F. B. Davies *et al*., Astrophys. J. **855**, 128 (2018)